Chemical Engineering Journal 524 (2025) 169132

Contents lists available at ScienceDirect

Chemical Engineering Journal

journal homepage: www.elsevier.com/locate/cej

Atomic dispersion of scandium in electrochemically reduced copper oxide nanosheets for efficient electrocatalytic CO_2 reduction to C_{2+} products

Yang Zhao [a,b,c,1], Binwen Zeng [d,1], Haoliang Huang [a,1], Huanhuan Yang [a,b], Zhipeng Yu [e], Chao Song [a], Jingwei Wang [a,b], Kaiyang Xu [a], Xinyi Xiang [a], Wei Wang [a,b], Fei Lin [a], Sheng Meng [a,b], Lijian Meng [f], Zhiming Cui [d,*], Lifeng Liu [a,*]

[a] Songshan Lake Materials Laboratory (SLAB), Dongguan, 523808, China
[b] Institute of Physics, Chinese Academy of Sciences, Beijing, 100190, China
[c] Guangdong University of Science and Technology, Dongguan, 523083, China
[d] Guangdong Provincial Key Laboratory of Fuel Cell Technology, School of Chemistry and Chemical Engineering, South China University of Technology, Guangzhou, 510641, China
[e] International Iberian Nanotechnology Laboratory (INL), 4715-330, Braga, Portugal
[f] Centre of Innovation in Engineering and Industrial Technology, Instituto Superior de Engenharia do Porto, Instituto Politecnico do Porto, 4249-015, Porto, Portugal

ARTICLE INFO

Keywords:
Electrochemical CO_2 reduction
Rare earth doping
CuO nanosheet
Strain engineering
Surface reconstruction

ABSTRACT

Converting CO_2 into value-added chemicals and fuels through electrochemical CO_2 reduction reaction (CO_2RR) has been acknowledged as a disruptive technology for chemical industry and an important means to realizing carbon neutrality. However, it remains challenging to achieve high selectivity for C_{2+} products at a large current density with a low overpotential. Herein, we report a scandium (Sc) single-atom-doped CuO nanosheet (Sc_1CuO NS) electrocatalyst for efficient and durable CO_2-to-C_{2+} conversion. The optimal Sc_1CuO NS catalyst achieves a maximal C_{2+} Faradaic efficiency of 73 ± 1.8 % at 475.2 mA cm^{-2} under an ultralow potential of −0.6 *V* versus the reversible hydrogen electrode (RHE) and maintains stable CO_2-to-C_{2+} conversion at ~206 mA cm^{-2} with a > 60 % Faradaic efficiency for 47 h without degradation. In-situ spectroscopy measurements combined with density functional theory (DFT) calculations reveal that the electron transfer from Sc to Cu enhances the activation of CO_2 to *CO. Moreover, the in-situ electrochemical reduction of CuO generates abundant undercoordinated Cu^0 sites, featuring tensile-strained Sc-(O)-Cu motifs, which serve as active centers that reduce the reaction barrier for C—C coupling. This work highlights the importance of rare-earth doping combined with in-situ electrochemical surface reconstruction of CuO as an effective catalyst design strategy to boost CO_2-to-C_{2+} conversion performance.

1. Introduction

Renewable energy driven electrocatalytic carbon dioxide (CO_2) reduction (CO_2RR) represents an eco-friendly approach to valorizing the notorious anthropogenic CO_2 emissions to highly valuable multicarbon (C_{2+}) products like ethylene and ethanol [1,2], which has been widely recognized as a promising way of contributing to carbon neutrality. The key to realizing CO_2-to-C_{2+} conversion is to develop high-performance copper (Cu) based CO_2RR electrocatalysts with high selectivity toward C_{2+} products [3,4], considering that Cu is by far the only metal enabling efficient electrochemical conversion of CO_2 to C_{2+} commodities. Among many Cu-based CO_2RR electrocatalysts, the oxide-derived Cu (OD-Cu) has recently drawn considerable attention because OD-Cu typically possesses abundant defective grain boundaries and undercoordinated Cu sites stemming from the removal of oxygen from the lattice of copper oxide (CuO/Cu_2O), which can facilitate the dimerization of the *CO intermediate and stabilize $*C_2$ species, driving the reaction to proceed along the pathway of C_{2+} generation. Notwithstanding some progress [5–7], the OD-Cu catalysts reported so far still face substantial limitations, such as high reaction overpotentials at high current densities, unsatisfactory selectivity for C_{2+} compounds, and relatively complex procedures for surface reconstruction. This is largely because the

* Corresponding authors.
E-mail addresses: zmcui@scut.edu.cn (Z. Cui), liu.lifeng@sslab.org.cn (L. Liu).
[1] These authors contributed equally to this work.

https://doi.org/10.1016/j.cej.2025.169132
Received 14 July 2025; Received in revised form 28 September 2025; Accepted 29 September 2025
Available online 30 September 2025

undercoordinated Cu sites induced by the electrochemical reduction of CuO/Cu_2O alone are not sufficient to optimize the adsorption strength of key intermediates (e.g., *CO or *OCCO) and effectively control the kinetics of C—C coupling. Therefore, it is highly preferable to combine the in-situ electrochemical reduction for OD-Cu preparation with other catalyst design strategies such as heteroatom doping [8,9], surface and interface modification [10–13], and strain and defect engineering [14–16], to synergistically tune the electronic structure and local coordination environment, so that the constraints imposed by the linear scaling relations can be overcome and high CO_2-to-C_{2+} activity and selectivity be favorably achieved at a low potential with a high current density.

To this end, rare-earth (RE) element doping in or alloying with Cu-based catalysts has emerged as an effective method, because on one hand, the introduction of large RE atoms (e.g., lanthanium (La), scandium (Sc), and yttrium (Y)) into Cu-based catalysts may cause tensile lattice strain, helping to regulate Cu—O bond lengths and d-band center positions, thereby enhancing CO_2 adsorption and activation capabilities [17,18]; on the other hand, the distinctive 4f orbital structures and lanthanide contraction effect of RE elements can localize electrons and regulate the adsorption capability of reaction intermediates, improving the catalytic performance for CO_2RR [19,20]. Indeed, recent studies have showed that doping Cu-based catalysts with RE elements such as La, samarium (Sm), cerium (Ce), praseodymium (Pr) and erbium (Er), markedly boosted the CO_2RR activity [21–24]. For instance, doping La into Cu hollow spheres was demonstrated to promote the formation of *CO intermediates at Cu sites and lower the energy barrier to the C—C coupling, therefore resulting in a high activity for CO_2-to-C_{2+} conversion under strongly acidic conditions [25]. Similarly, Feng et al. introduced single-atom gadolinium (Gd) into Cu_2O to obtain Gd_1/CuO_x catalysts [26]. They found that the Gd atoms singly dispersed in CuO_x not only helped to maintain the stability of Cu^+ species during the reaction but also induced tensile lattice strain, which stabilized the critical *OCCO intermediate and reduced the energy barrier to C—C coupling. Although the promotional effect of RE elements in electrocatalytic CO_2RR has been documented [27,28], the RE doping strategy remains largely unexplored in the oxide-derived Cu-based catalysts. Therefore, developing novel RE-doped OD-Cu catalysts and elucidating the correlation between their dynamic structural evolution and catalytic activity are of essential significance for advancing electrochemical CO_2RR research.

In this work, we developed Sc-doped CuO nanosheet (NS) catalysts with different concentrations of Sc dopants through a facile hydrothermal method. Comprehensive atomic structure characterization confirmed that Sc is doped into the CuO crystal lattice in the form of isolated single atoms (hereafter denoted as Sc_1CuO). When used to catalyze the CO_2RR, CuO is electrochemically reduced forming the OD-Cu having abundant undercoordinated transient Cu^0 sites, which couple with the atomically doped Sc making the Sc-(O)-Cu become the active centers for CO_2-to-C_{2+} conversion. As a result, the Sc_1CuO catalyst with an optimal concentration of 1.6 wt% Sc, i.e., Sc_1CuO-1.6, can achieve a maximal C_{2+} Faradaic efficiency of 73 ± 1.8 % at a high current density of 475.2 mA cm^{-2} under an ultralow applied potential of −0.6 *V* versus the reversible hydrogen electrode (RHE). Moreover, Sc_1CuO-1.6 is able to maintain a stable current density of ~206 mA cm^{-2} under −0.5 V vs. RHE for 47 h without degradation, demonstrating outstanding durability. Operando X-ray absorption spectroscopy (XAS) and Raman spectroscopy experiments as well as density functional theory (DFT) calculations reveal that the lattice strain induced by Sc doping and surface reconstruction upon the electrochemical reduction enhances the adsorption and activation of CO_2, and the formed Sc-(O)-Cu active sites notably reduce the energy barrier for C—C coupling, thereby promoting efficient CO_2 reduction to C_{2+} products. Our work demonstrates the effectiveness of rare-earth doping and in-situ electrochemical surface reconstruction of CuO in promoting the activity and stability of CO_2RR to C_{2+} products.

2. Experimental section

2.1. Synthesis of Sc-doped CuO nanosheet catalysts

In a typical procedure, the Sc-doped CuO NSs were prepared by the hydrothermal method [29], using $Cu(NO_3)_2$ as the copper source. Specifically, 2 mL of 3.0 M NaOH solution were dropped into 2 mL of 1.0 M $Cu(NO_3)_2$ solution. Subsequently, 0.08 mmol $Sc(NO_3)_3{\cdot}6H_2O$ was added into the above mixed solution, which was then stirred vigorously for 1 h. Afterward, the mixture was transferred into a 5 mL Teflon-lined stainless-steel autoclave reactor and heated at 120 °C for 4 h. After cooling the reactor to room temperature, the solution was subjected to centrifugation, washed 5 times with a mixture of deionized (DI) water and ethanol (v/v: 1:1), and then dried at 60 °C for 6 h in a vacuum oven. The control catalysts with different Sc/Cu ratios were synthesized by the same procedure, except that the amount of $Sc(NO_3)_3{\cdot}6H_2O$ precurosr used was 0.02 mmol for Sc_1CuO-0.5 and 0.16 mmol for Sc_1CuO-3.8. The CuO NS benchmark was prepared following the same procedure without the $Sc(NO_3)_3$ addition.

2.2. Electrocatalytic measurements

All electrochemical CO_2RR experiments were conducted in a commercial flow cell separated by an anion exchange membrane (PiperION-A20). Each compartment was filled with 50 mL of 1.0 M KOH electrolyte. A Pt foil and a Hg/HgO electrode served as the counter and reference electrodes, respectively. All electrode potentials are converted to the RHE scale using the formula $E_{RHE} = E_{Hg/HgO} + 0.098\ V + 0.0591 \times$ pH. 85 % iR correction was applied to compensate the iR drop between the working electrode and the reference electrode. Before conducting electrochemical tests, the catalyst-loaded gas diffusion electrode (GDE, YLS-30 T, Suzhou Sinero Company) was conditioned at −100 mA cm^{-2} for 10 min. Linear sweep voltammetry (LSV) curves were recorded using the CS-310MA electrochemical workstation (Wuhan CorrTest Instrument Co. Ltd.) at a scan rate of 10 mV s^{-1}. Chronoamperometry (CA) tests were conducted at each potential for 20 min. Current densities were normalized to the geometric surface area of the electrode (i.e., 1 cm^2). CO_2 gas was fed into the cathodic compartment at a rate of 30 sccm and injected online into the gas chromatograph (GC, BFRL-SP-3530). For long-term stability tests, PTFE emulsion (DISP-30, DuPont) was sprayed onto the gas diffusion layer (GDL) side of the GDE with a loading of ~1 mg cm^{-2}. The FTFE-coated GDE was then annealed in a muffle furnace at 380 °C for 30 min for further use. A homogeneous catalyst ink was prepared by blending 20 mg of catalysts, 20 μL of PTFE emulsion, 2 mL of isopropanol and 80 μL of Nafion® solution (5 % in ethanol), followed by sonication for 30 min. Afterward, the catalyst ink was air-brushed onto the non-GDL side of the GDE with a mass loading of 2 mg cm^{-2}.

The gaseous products (H_2, CO, C_2H_4 and CH_4) were quantified by a GC (BFRL-SP3530) equipped with a flame ionization detector (FID) for CO, C_2H_4 and CH_4, and a thermal conductivity detector (TCD) for H_2. High-purity Ar (99.999 %) was used as the carrier gas. The Faradaic efficiency of each gaseous product was calculated by the following equation:

$$\mathrm{FE}\ (\%) = \frac{nzF}{Q} \times 100\% \quad (1)$$

where n is the mole fraction of the product, z stands for the number of electrons transferred for the product formation, $F = 96{,}485\mathrm{C\ mol^{-1}}$ is the Faraday constant, and Q represents the total charge passed.

Liquid products were quantified on the Bruker 400 MHz NMR spectrometer. Typically, 500 μL of the collected catholyte exiting the flow cell was mixed with 100 μL D_2O containing 20 ppm (m/m) dimethyl sulphoxide (≥ 99.9 %, Alfa Aesar) as the internal standard. The Faradaic efficiency was calculated as follows:

$$FE_{liquid}\ (\%) = \frac{Q_{liquid}}{Q_{total}} \times 100\% = \frac{m_{liquid} nF}{I \times t} \times 100\% \quad (2)$$

where m_{liquid} (mol) is the amount of liquid products generated, n is the number of transferred electrons for 1 mol product generation, I (A) is the measured current, and t (s) is the electrolysis time.

2.3. In-situ electrochemical surface-enhanced Raman spectroscopy (SERS) measurements

The SERS measurement was carried out on a Horiba LabRam HR Evolution Raman microscope using a commercial electrochemical cell with an optically transparent window (Fig. S1). The carbon paper loaded with catalysts was used as the working electrode (loading mass: 1 mg cm^{-2}), and a Ag/AgCl electrode and a Pt wire were used as the reference and counter electrodes, respectively. To enhance the Raman signals, shell-isolated gold nanoparticles (SHINs, i.e., Au@SiO_2, Xiamen SHINs Technology Co., Ltd.) were dispersed onto the working electrode surface with a loading of 4 μg cm^{-2}. 0.5 M $KHCO_3$ aqueous solution was used as the electrolyte and circulated through the cathodic and anodic compartments by peristaltic pumps at a rate of 10 mL min^{-1}. Since directly introducing CO_2 gas into the thin cell would cause turbulence affecting the measurement, CO_2-saturated electrolyte was continuously fed into the test cell (Fig. S1). Prior to electrochemical measurements, the catalyst-coated electrode was pre-conditioned at −0.6 *V* vs. RHE for 10 min. The potential range was set from the open circuit potential (OCP) to −1.0 V vs. RHE. A 633 nm laser was employed as the light source, and Raman signals were recorded with a 20 s integration and by averaging 2 consecutive scans.

3. Results and discussion

The synthesis of Sc_1CuO NS catalysts is schematically illustrated in Fig. 1a. In a typical procedure, the Sc-doped CuO NSs were prepared via a hydrothermal method using $Cu(NO_3)_2$ and $Sc(NO_3)_3$ as the copper and scandium sources, respectively. The mixture was transferred into a Teflon-lined stainless-steel autoclave and heated at 120 °C for 4 h (see Experimental details). To investigate how the Sc content influences the CO_2RR performance of Sc_1CuO NSs, precursor solutions with different concentrations of $Sc(NO_3)_3$, including 5, 20, and 40 mM, were prepared

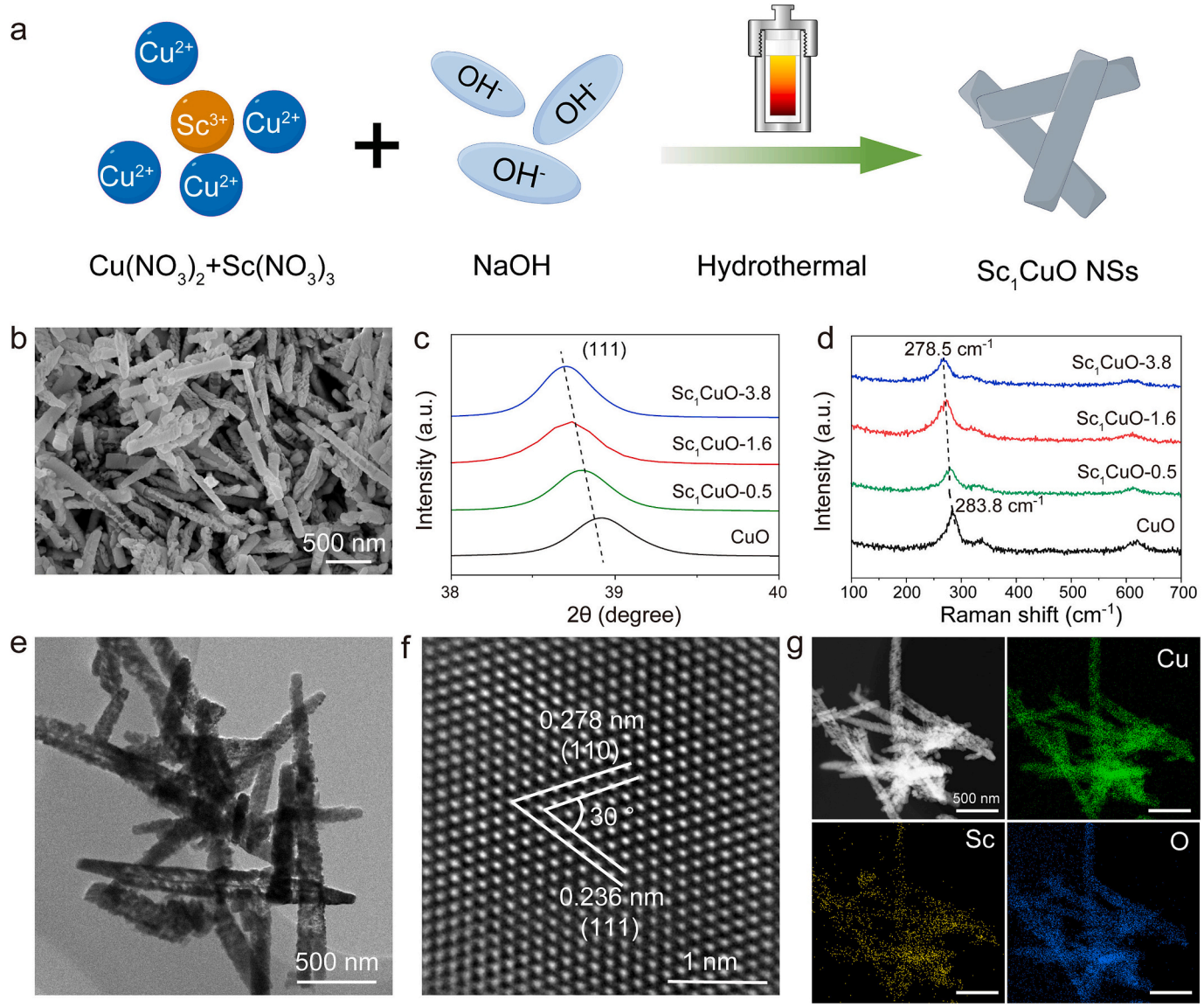

Fig. 1. (a) Schematic illustration of the synthesis of Sc_1CuO NSs. (b) Representative SEM image of Sc_1CuO-1.6. (c) Zoomed XRD patterns of Sc-doped CuO and pristine CuO in the range of 38° ~ 40°, showing the evolution of the (111) diffraction peak as the Sc content varies. (d) Raman spectra of all catalysts. (e) TEM image, (f) HRTEM image, and (g) HAADF-STEM image and corresponding elemental maps of Cu, Sc and O of Sc_1CuO-1.6 catalysts.

for the hydrothermal synthesis, which led to the Sc dopant content of 0.5, 1.6, and 3.8 wt%, respectively, as determined by inductively coupled plasma optical emission spectrometry (ICP-OES, Table S1). Based on these values, the samples are designated as Sc_1CuO-0.5, Sc_1CuO-1.6, and Sc_1CuO-3.8, respectively. Scanning electron microscopy (SEM) examination of samples revealed that the synthesized catalysts undergo a morphological transition from large nanosheet-like structures to small elongated nanorods (NRs) as the Sc content in CuO increases (Figs. 1b and S2). It is hypothesized that such morphological transformation may result from, on one hand, the Sc doping induced lattice strain that distorts some crystallographic directions more than others, altering the growth kinetics; on the other hand, the charge imblance arising from the replacement of Cu^{2+} by Sc^{3+}, which likely creates oxygen vacancies, lowering the symmetry and changing crystal growth into nanorod-like morphology. The powder X-ray diffraction (XRD) patterns of these Sc-doped CuO catalysts show that the primary diffraction peaks of Sc-doped CuO resemble closely those of the standard CuO reference (PDF#89–5899, Fig. S3). Notably, no distinct diffraction peaks arising from metallic Sc or scandium oxide (e.g., Sc_2O_3) were observed, suggesting that Sc is doped into the CuO lattice, likely in the form of atomic dispersion. Fig. 1c displays a zoomed view of the XRD patterns in the range of 38° ~ 40°, where the (111) diffraction peak of the Sc-doped CuO samples shifts toward the lower angle relative to that of pure CuO (~38.9°), indicating that the incorporation of Sc atoms into the CuO lattice introduces tensile strain. To further quantify the crystal structure changes, the Rietveld refinements were carried out (Fig. S4). Compared to the pristine CuO, the unit cell volume of Sc_1CuO expands from 81.29(5) $Å^3$ to 81.31(7), 81.36(6), and 81.38(2) $Å^3$ for Sc_1CuO-0.5, Sc_1CuO-1.6, and Sc_1CuO-3.8, respectively (Table S2), accompanied by minor variations in lattice parameters. This reaffirms that Sc atoms are indeed incorporated into the CuO lattice. Besides, Raman spectroscopy was performed, and the primary Cu—O vibrational band of CuO, located at 283.8 cm^{-1}, shifts toward the lower wavenumber (278.5 cm^{-1}) upon Sc doping (Fig. 1d) [30]; moreover, the intensity of the Cu—O vibration peak is also reduced. This indicates the substitution of bigger Sc^{3+} ions for Cu^{2+} ions, and the associated charge imblance leads to a larger Cu—O bond length with weakened Cu—O bonding, consistent with the tensile lattice strain confirmed by XRD.

The microstructure and composition of Sc-doped CuO and pristine CuO were further investigated by transmission electron microscopy (TEM). The pristine CuO shows a well-defined nanosheet structure with a relative smooth surface (Fig. S5a). When a little Sc is introduced into CuO (Sc_1CuO-0.5), the NS-like architecture remains (Fig. S5d). However, as the Sc content increases, the samples are gradually transformed into elongated NSs and NRs; moreover, the sample surface becomes rough (see Fig. 1e for Sc_1CuO-1.6 and Fig. S5g for Sc_1CuO-3.8). The high-resolution TEM (HRTEM) image reveals a lattice spacing of 2.74 Å in pristine CuO catalysts (Fig. S5b), corresponding to the (110) crystal planes. Upon doping with Sc, the lattice distance of (110) planes increases to 2.75 Å, 2.78 Å, and 2.80 Å for Sc_1CuO-0.5, Sc_1CuO-1.6, and Sc_1CuO-3.8, respectively (Figs. 1f, S5e and S5h), corresponding to a lattice expansion value (ε) of around 0.4 %, 1.5 %, and 2.2 %, which is attributed to the tensile strain induced by the incorporation of the larger Sc atoms (~162 pm) into the CuO lattice. Energy-dispersive X-ray spectroscopy (EDS) mapping analysis under TEM further confirmed the homogeneous dispersion of Cu, Sc and O elements within the Sc_1CuO-1.6 catalyst (Fig. 1g). Additionally, the geometric phase analysis (GPA) was employed to quantitatively assess the lattice strain distribution, based on the HRTEM images acquired. The resulting strain maps clearly show that all Sc-doped CuO catalysts exhibit different magnitudes of tensile strain on the nanometer scale (Figs. S5f, S5j and S6), compared to that of the pristine CuO (Fig. S5c), which unambiguously validate the effectiveness of the Sc doping approach in introducing lattice strain in CuO catalysts.

The surface chemistry of the Sc-doped CuO catalysts was further investigated by X-ray photoelectron spectroscopy (XPS). The Cu 2p core-level XPS spectra of all samples exhibit prominent satellite peaks (Fig. 2a), which are characteristic of the Cu^{2+} oxidation state [31]. Notably, the binding energy of the Cu $2p_{3/2}$ peak in Sc_1CuO-3.8 shifts toward the lower value compared to that of the pristine CuO (Fig. 2a), which can be attributed to the charge transfer from Sc to Cu, resulting likely from the higher electronegativity of Cu (1.90) relative to that of Sc (1.36). Further analysis of the Cu LMM Auger spectra reveals that the surface Cu exists in the Cu^{2+} oxidation state for all Sc-doped CuO as well as the pristine CuO samples (Fig. 2b) [9]. According to the Sc 2p XPS spectra, Sc_1CuO-1.6 and Sc_1CuO-3.8 exhibit a similar spin-orbit splitting energy ($\Delta E = 4.4$ eV), indicating that the Sc species exist in an oxidized state (Fig. 2c) [17]. However, the binding energy of Sc_1CuO-3.8 shifts toward the higher value with respect to that of Sc_1CuO-1.6, implying that more electrons transfer from Sc to Cu in Sc_1CuO-3.8, in agreement with the Cu 2p XPS spectra. It is also noted that there are no detectable XPS signals for Sc_1CuO-0.5, owing to the ultralow Sc content in this catalyst.

Furthermore, X-ray absorption spectroscopy was employed to analyze the electronic structure and local coordination environments of all samples. The Cu K-edge X-ray absorption near-edge spectrum (XANES) of Sc_1CuO-1.6 closely resembles that of CuO (Fig. 2d), suggesting that the chemical state of Cu species in the catalysts is Cu^{2+}, consistent with the XPS analysis. The Fourier transform (FT) of the extended X-ray absorption fine structure (EXAFS) spectrum for Sc_1CuO-1.6, presented in Fig. 2e, shows a dominant peak in R space at ~1.5 Å, attributed to the nearest-shell Cu—O coordination, and another weaker signal at ~2.5 Å is assigned to the second-shell Cu-(O)-Cu contribution [22]. It is noteworthy that both the Cu—O and Cu-(O)-Cu scattering paths shift to a higher R value with respect to those of CuO, indicating an increased bond length induced by the tensile lattice strain, in line with the XRD and Raman spectroscopy results (Fig. 1c-d). Additionally, the wavelet transform (WT) analysis of the EXAFS spectra that reveals the coordination in both R- and k-spaces more intuitively, was also carried out (Fig. 2f). The WT contour for Sc_1CuO-1.6 exhibits a maximum at 6.4 $Å^{-1}$, which is assigned to Cu—O coordination. In the high R range (above 2.5 Å), the presence of Cu-(O)-Cu coordination is also observed. At the Sc K-edge, the XANES spectra of all Sc_1CuO samples show a similar profile, which is distinct from that of Sc_2O_3, suggesting that Sc is incorporated into the lattice of CuO and no separate Sc_2O_3 forms (Fig. 2g). The FT-EXAFS of the pristine Sc_2O_3 confirms the presence of Sc—O (~1.6 Å) and Sc-(O)-Sc bonding (~3.0 Å) in the first and second coordination shells (Fig. 2h), respectively. In contrast, the signal of Sc-(O)-Sc scattering is absent in the FT-EXAFS spectra of all Sc-doped CuO samples, indicating that Sc exists as isolated atoms in the CuO lattice without metal-metal coordination. Likewise, the WT contour of Sc_1CuO-1.6 exhibits only one maximum at 6.1 $Å^{-1}$, attributed to Sc—O coordination (Fig. 2i), and no signal corresponding to Sc-(O)-Sc coordination can be resolved, further confirming that Sc is atomically dispersed in Sc_1CuO-1.6. In this way, Sc atoms substitute Cu atoms forming Sc—O sites that exert a tensile strain on the lattice.

The electrocatalytic CO_2RR performance of the Sc-doped CuO catalysts was evaluated in an alkaline flow cell equipped with the gas-diffusion electrode (GDE, Fig. S7). All potentials are converted to the RHE scale with an iR correction of 85 %. Fig. 3a shows the linear sweep voltammetry (LSV) curves of all samples under investigation, where the Sc-doped CuO catalysts exhibit higher current densities than the pristine CuO at a given applied potential, indicating that Sc doping indeed enhances the CO_2RR activity. In particular, Sc_1CuO-1.6 shows better CO_2RR performance than Sc_1CuO-0.5 and Sc_1CuO-3.8, able to reach the cathodic current density of 1.0 A cm^{-2} at a comparatively low potential of only −0.88 *V* vs. RHE under a constant CO_2 flow (30 sccm), suggesting that 1.6 wt% is an optimal dopant content. Both gas and liquid products were analyzed by gas chromatograph (GC) and nuclear magnetic resonance (NMR) spectroscopy (Fig. S8). The calibration curves for the liquid products of CO_2RR catalyzed by Sc_1CuO-1.6 are presented in Fig. S9. Fig. 3b reveals the product distribution for the best-performing

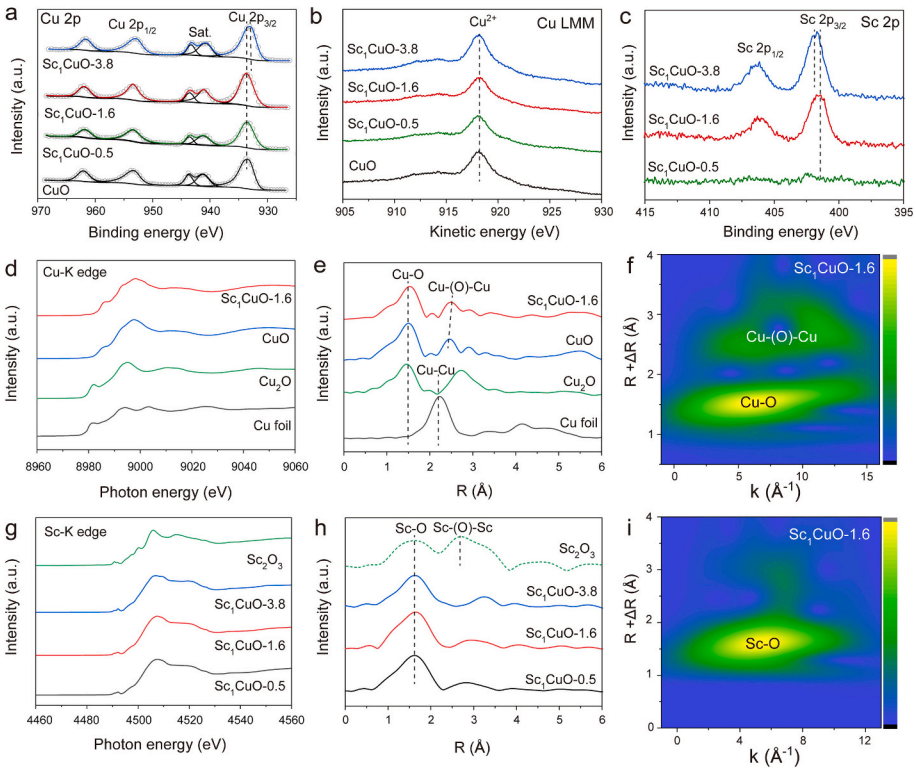

Fig. 2. XPS spectra of (a) Cu 2p, (b) Cu LMM Auger and (c) Sc 2p core-levels for all catalysts. (d) Cu K-edge XANES spectra and (e) FT-EXAFS spectra of Sc_1CuO-1.6 and other controls. (f) The WT-EXAFS contour of Sc_1CuO-1.6 at Cu K-edge. (g) Sc K-edge XANES spectra and (h) FT-EXAFS spectra of all Sc_1CuO catalysts and the Sc_2O_3 control. (i) The WT-EXAFS contour of Sc_1CuO-1.6 at Sc K-edge.

Sc_1CuO-1.6, where C_{2+} compounds (i.e., C_2H_4 and C_2H_5OH) predominate among all multi-carbon products. The Faradaic efficiency (FE) values of Sc_1CuO-1.6 for different products are plotted as a function of the applied cathodic potential, displaying that the FE for C_{2+} production first increases as the potential becomes more negative, peaking at -0.6 *V* vs. RHE, and then gradually decreases. Remarkably, Sc_1CuO-1.6 exhibits exceptional selectivity for C_{2+} products, achieving a maximal FE of 73 $\pm$ 1.8 % at -0.6 V vs. RHE. It is worth noting that this applied potential is significantly lower than that of other copper oxide-derived electrocatalysts reported recently in the literature (Table S3).

Furthermore, the impact of Sc doping in Sc_1CuO catalysts on the CO_2RR performance was investigated. Overall, the Sc doping substantially improves the FE of catalysts toward C_{2+} production (Fig. 3c), compared to the pristine CuO, and Sc_1CuO-1.6 shows the highest FE (C_{2+}) among others, capable of maintaining a FE for C_{2+} products above 60 % over a potential range from -0.5 to -0.8 V vs. RHE, markedly outperforming Sc_1CuO-0.5 and Sc_1CuO-3.8 (Fig. S10). Fig. 3d shows the partial current density for C_{2+} products (j_{C2+}) of all catalysts at different potentials. Sc_1CuO-1.6 exhibits an impressive partial current density of 346.9 mA cm^{-2} for C_{2+} products at -0.6 V vs. RHE, which is 3.9, 1.6, and 2.0 times higher than that of pure CuO (87.6 mA cm^{-2}), Sc_1CuO-0.5 (209.1 mA cm^{-2}), and Sc_1CuO-3.8 (170.9 mA cm^{-2}), respectively, at the same potential. These results suggest that the optimal Sc doping into CuO NSs significantly enhances both the activity and C_{2+} selectivity of the CO_2RR.

To elucidate the superior performance of Sc-doped CuO NS catalysts, additional experiments were carried out. The CO_2 adsorption experiments show that the Sc_1CuO-1.6 catalyst has much better capability of CO_2 adsorption than the pristine CuO, Sc_1CuO-0.5 and Sc_1CuO-3.8 controls (Fig. S11), which would lead to CO_2 enrichment near the local electrode surface when it is used to catalyze CO_2RR, thereby promoting CO_2 adsorption and activation [32,33]. The nitrogen (N_2) adsorption/desorption isotherms reveal that Sc_1CuO-1.6 possesses a higher specific surface area (14.7 m^2 g^{-1}) than Sc_1CuO-0.5 (11.6 m^2 g^{-1}), Sc_1CuO-3.8 (12.5 m^2 g^{-1}), and pristine CuO (10.2 m^2 g^{-1}), based on the Brunauer-Emmett-Teller (BET) method (Fig. S12a). Moreover, Sc_1CuO-1.6 has more mesopores compared to other controls (Fig. S12b). Additionally, the electrochemically active surface area (ECSA) was also determined based on the electrochemical double-layer capacitance (C_{dl}) method. Notably, the Sc_1CuO-1.6 catalyst exhibits an ECSA as high as 361.6 cm^2 (Fig. S13), approximately 1.8 times greater than that of pristine CuO (196.6 cm^2), suggesting that the exposure of more active sites contributes to the high CO_2RR activity of Sc_1CuO-1.6. Furthermore, the electrochemical impedance spectroscopy (EIS) measurements were performed to investigate the interfacial charge transfer behavior. Among all catalysts, Sc_1CuO-1.6 exhibits the lowest charge transfer resistance (R_{ct}), indicating enhanced electron transfer at the catalyst/electrolyte interface, which favorably accelerates the CO_2RR kinetics (Fig. S14, Table S4). Overall, the observed outstanding CO_2RR activity in Sc_1CuO-1.6 is the result of synergistic effects of electronic structure that provides reaction intermediates with favorable adsorption strength and material's physical properties (e.g., specific surface area, CO_2 adsorption capability) that facilitate mass transport of reactants and products. Besides, the long-term stability of the Sc_1CuO-1.6 for CO_2RR was assessed at a fixed potential of -0.5 *V* vs. RHE (Fig. 3e). Impressively, Sc_1CuO-1.6 maintains a stable current density of ~206 mA cm^{-2} with a FE of ~60 % toward C_{2+} production over 47 h without noticeable degradation, demonstrating excellent durability.

To gain insights into the morphology and surface chemistry changes after the long-term stability test, the post-mortem analyses of Sc_1CuO-1.6 were carried out using SEM, TEM, and XPS. SEM examination revealed that the elongated nanosheet morphology virtually remained unchanged (Fig. S15a). However, upon close inspection, fragmentation of nanosheets was observed, accompanied by surface reconstruction (Fig. S15b), which likely serves as the actual catalytically active surfaces during CO_2RR. Further SEM-EDS analysis showed that the Sc element

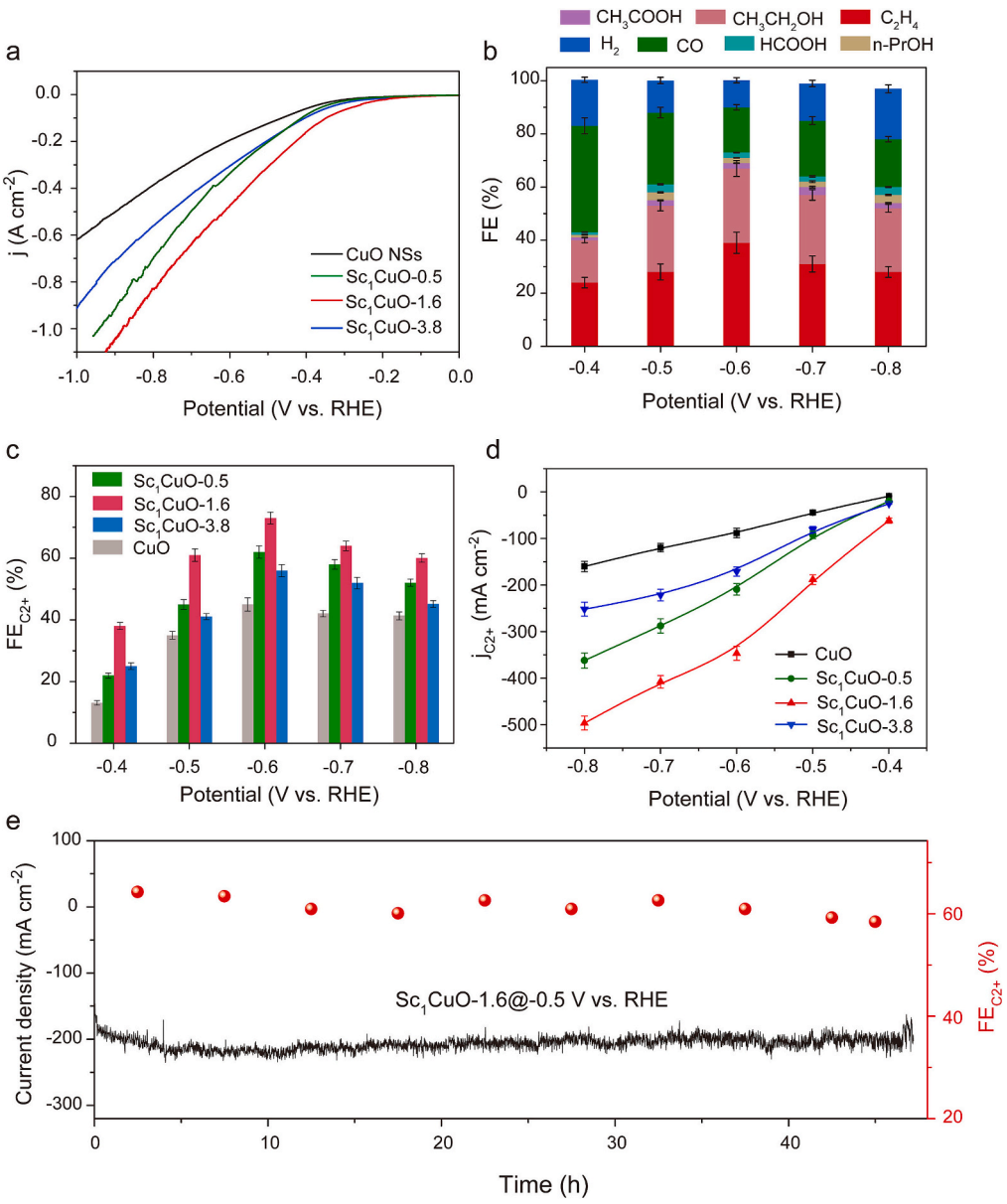

Fig. 3. (a) LSV curves of Sc_1CuO-1.6 and other control samples. (b) Potential-dependent Faradaic efficiency (FE) of various products for Sc_1CuO-1.6. (c) Comparison of the C_{2+} FE values at different potentials for different catalysts. (d) Partial current density of Sc_1CuO-1.6 and other control samples as a function of the applied potential. (e) Long-term stability of the Sc_1CuO-1.6 catalyst at −0.5 *V* vs. RHE.

was still retained after extended CO_2RR at a high current density (Fig. S15c). The post-mortem XPS analysis revealed that the strong Cu 2p satellite peak (~942.5 e*V*) disappeared after the stability test, suggesting the reduction of Cu^{2+} to Cu^0/Cu^+ (Fig. S16a). Moreover, new peaks appeared at 919 and 917 eV, assigned to Cu^0 and Cu^+ species, respectively, as evidenced from the Cu LMM Auger spectrum after the stability test (Fig. S16b), reaffirming the reduction of Cu^{2+} species. As for the Sc 2p XPS spectrum, no discernible changes in binding energy were observed before and after the stability test, manifesting that the chemical state of Sc was not altered during CO_2RR (Fig. S16c). Overall, the post-mortem analyses further validate the outstanding catalytic stability of Sc_1CuO-1.6, substantiating its potential for practical applications.

To further understand how the Cu valence state and coordination environment dynamically change during CO_2RR, in-situ XAS was conducted at different applied potentials. Fig. 4a presents the Cu K-edge XANES spectra of the Sc_1CuO-1.6 catalyst under the CO_2RR conditions, which were acquired by progressively decreasing the potential from the open circuit potential (OCP) to −0.6, −0.8 and − 1.0 *V* vs. RHE. For comparison, the XANES spectra of pristine Cu foil and CuO are also given as references. At OCP, the absorption edge of Sc_1CuO-1.6 virtually overlaps with that of CuO, suggesting that the initial oxidation state of Cu in Sc_1CuO-1.6 is 2+. When a cathodic potential is applied, the absorption edge shifts notably toward the lower energy, exhibiting a feature similar to that of Cu foil, indicating the reduction of Cu^{2+} to metallic Cu [34,35]. According to FT-EXAFS spectra, Sc_1CuO-1.6 at OCP resembles that of CuO, showing a dominant signal at 1.5 Å that corresponds to Cu—O coordination (Fig. 4b). When a potential of −0.4 V vs. RHE is applied, a peak associated with Cu—Cu coordination appears, but the Cu—O signal is still visible (Fig. S17), indicating partial reduction of Cu^{2+} species to Cu^0 in Sc_1CuO-1.6. Interestingly, although the Cu—O signal completely vanishes at more negative applied potentials (Fig. 4b), it immediately re-appears when the applied potential returns to OCP (Fig. S17). This suggests that the coordination environment and chemical state of Cu undergo a dynamic change and the completely reduced Cu^0 is most likely a transient state during CO_2RR. To make quantitative

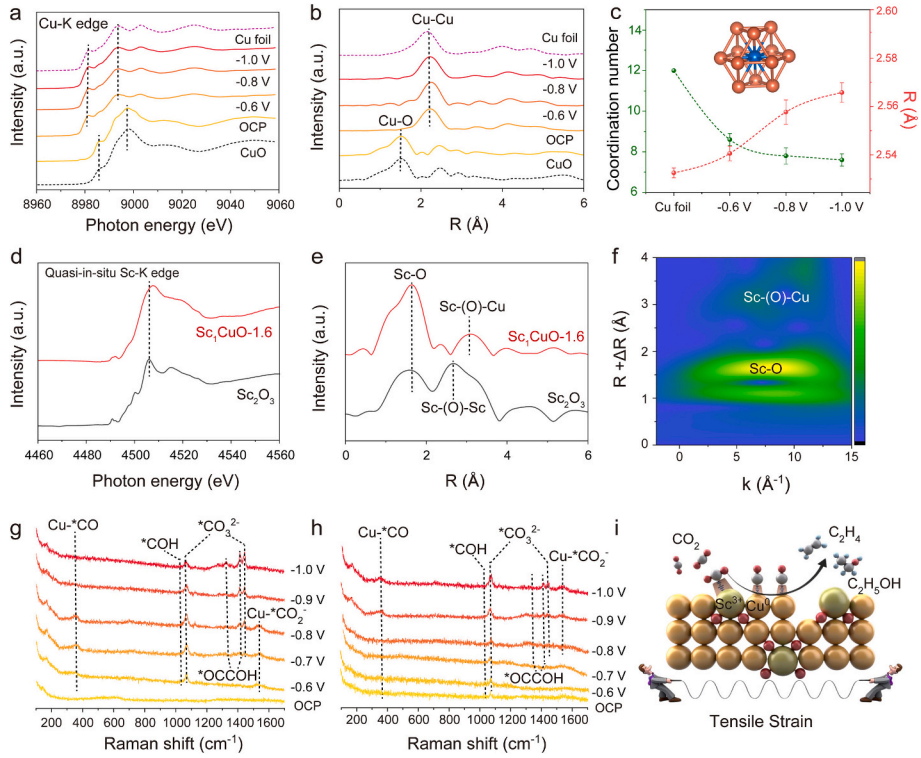

Fig. 4. (a) In-situ Cu K-edge XANES spectra, (b) FT-EXAFS spectra and (c) the corresponding coordination numbers and bond distances of Sc_1CuO-1.6 measured under different potentials. The inset in panel (c) is a scheme illustrating the Cu crystal with a perfect coordination structure (CN = 12). (d) Quasi-in-situ Sc K-edge XANES spectra, (e) the corresponding FT-EXAFS spectra and (f) WT-EXAFS contour of Sc_1CuO-1.6 after the CO_2RR at −0.8 *V* vs. RHE. In-situ surface-enhanced Raman spectra of (g) Sc_1CuO-1.6 and (h) pristine CuO recorded at different potentials. (i) Schematic illustration of the CO_2 conversion into C_{2+} products on the reconstructured Sc_1CuO catalyst, highlighting the roles of tensile strain and defects.

comparison, the changes in Cu coordination number (CN) and Cu—Cu bond distance are plotted as a function of the applied potential upon FT-EXAFS fitting (Fig. S18 and Table S5), with those of the Cu foil included as a reference (Fig. 4c). The pristine Cu foil has a CN of 12 and a Cu—Cu bond length of 2.534 Å. Upon electrochemical reduction under a cathodic potential, the Cu—Cu coordination number in Sc_1CuO-1.6 is substantially lowered, confirming the formation of defect-rich undercoordinated Cu sites during electroreduction [36,37]. Moreover, the Cu—Cu bond length in Sc_1CuO-1.6 is expanded, indicating additional tensile strain superimposed on that induced by Sc doping [16,36]. Besides, it is also noted that as the applied potential becomes more negative, the CN further reduces and the Cu—Cu bond length increases, showing an opposite variation trend.

Due to the low Sc content in Sc_1CuO-1.6 and the strong X-ray absorption by the electrolyte and electrochemical cell window in the low energy range, it is very challenging to perform operando XAS experiments at Sc K-edge, if possible at all. Therefore, quasi-in-situ Sc K-edge XAS measurements were conducted by collecting the spectra immediately after the CO_2RR testing. Interestingly, as shown in Fig. 4d, the quasi-in-situ XANES spectrum is similar to that of Sc_2O_3 even after the CO_2RR under a cathodic potential of −0.8 *V* vs. RHE, which implies that Sc is not reduced and remains in the initial oxidation state during CO_2RR, in good agreement with the post-mortem XPS results (Fig. S16c). Both FT-EXAFS spectrum and WT contour reveal that while the signal of Sc—O coordination predominates, that of Sc-(O)-Cu coordination begins to appear after CO_2RR (Fig. 4e-f). Therefore, two distinct coordination sites are identified in Sc_1CuO-1.6, namely, the Sc^{3+}-O site near the atomically dispersed Sc atom and the Sc-(O)-Cu site located in the second shell from the Sc atom and surrounded by Cu atoms [22]. Based on the above analyses, undercoordinated Cu^0 species formed during the in-situ electrochemical reduction of CuO, featuring a tensile-strained Sc-(O)-Cu coordination site, is believed to be the true catalytically active site for CO_2RR, which is expected to facilitate CO_2 adsorption and promote its further reduction to C_{2+} products.

Additionally, in-situ surface-enhanced Raman spectroscopy (SERS) was conducted to investigate the adsorption behavior of reaction intermediates, aiming at clarifying the origin of the formation of more C_{2+} products on the reconstructed Sc_1CuO-1.6 surface. Fig. 4g and h display the Raman spectra collected from the surfaces of Sc_1CuO-1.6 and CuO catalysts during the reaction at different applied potentials ranging from OCP to −1.0 V vs. RHE. In all cases, no peaks arising from surface copper oxides (i.e., CuO and Cu_2O) are observed, corroborating the reduction of these oxides to Cu^0. The signals of $*CO_3^{2-}$ at 1068 and 1443 cm^{-1} originate from the deprotonation of HCO_3^-, which indicates an enhanced local OH^- concentration on catalyst surfaces that can facilitate CO_2 activation and subsequent reduction steps [38,39]. The integral area of $*CO_3^{2-}$ peaks for Sc_1CuO-1.6 is significantly higher than that for pristine CuO (Fig. S19), suggesting higher local pH near the surface of Sc_1CuO-1.6 that can make CO_2 activation easier. In addition, the Cu-$*CO_2^-$ signal appearing at 1536 cm^{-1} reflects direct adsorption of dissolved CO_2 on catalyst surfaces [40–42]. For Sc_1CuO-1.6, the Cu-$*CO_2^-$ signal begins to appear at a potential as early as −0.6 V vs. RHE, while for CuO the signal does not emerge until a potential of −0.9 V vs. RHE is applied, which manifests that CO_2 can absorb more easily on Sc_1CuO than on CuO, in agreement with the CO_2 adsorption isotherms shown in Fig. S11. Importantly, the stretching vibration of Cu-*CO bonding is clearly observed at ~345 cm^{-1} on Sc_1CuO-1.6 in the potential range of −0.6 V to −0.8 V vs. RHE [43]. In contrast, for pristine CuO, the Cu-*CO stretching mode only emerges at −0.9 and − 1.0 V vs. RHE (Fig. 4h). This observation demonstrates that the activation of CO_2 to *CO via the $*CO_3^{2-}$/$*CO_2^-$ adsorption pathway on Sc_1CuO-1.6 is thermodynamically more favorable than that on pristine CuO. Furthermore, Raman signals arising from *OCCOH (1330 and 1414 cm^{-1}), a critical intermediate in C—C coupling [44,45], begin to appear at −0.7 V vs. RHE on Sc_1CuO-

1.6, much earlier than those on the CuO surface (only from −0.9 V vs. RHE onwards). Based on the in-situ XAS and SERS characterization, it is believed that the superior catalytic performance of Sc_1CuO-1.6 toward CO_2RR originates from: on one hand, the Sc doping that introduces tensile strain into the reduced CuO lattice and stabilizes high-valence Sc^{3+} species, which enhances the adsorption of CO_2 and promoting *CO formation; on the other hand, the in-situ reconstruction of the Sc_1CuO-1.6 surface under a cathodic potential that generates abundant undercoordinated Cu^0 defect sites, facilitating *CO dimerization to *OCCOH intermediates and thereby improving C_{2+} selectivity during CO_2RR (Fig. 4i).

DFT calculations were further performed to elucidate the effects of Sc doping and tensile strain on the catalytic behavior of Sc_1CuO-1.6 during the CO_2RR. To simulate the partial reduction of CuO under working conditions, two layers of oxygen atoms were removed from the CuO surface (Fig. S20). Moreover, to evaluate the strain effect on Sc-doped CuO, two Sc_1CuO model catalysts were constructed, one without lattice strain (i.e., 0 % lattice strain) and another with 1.5 % tensile strain, which are denoted as Sc_1CuO (0 %) and Sc_1CuO (1.5 %), respectively. The charge density difference of the surface adsorbed with *OCCO was first calculated for surface-reconstructed CuO, Sc_1CuO (0 %) and Sc_1CuO (1.5 %). As shown in Figs. 5a-c, significant redistribution of electron density occurs upon *OCCO adsorption on all catalyst surfaces. Notably, the Sc_1CuO (1.5 %) surface exhibits the strongest interaction with *OCCO intermediates, demonstrating the synergistic effect of Sc doping and introduced tensile strain. Besides, bader-charge analysis reveals that more electrons transfer from Sc_1CuO (1.5 %) to the adsorbent (0.96 e^-), compared to the CuO (0.38 e^-) and Sc_1CuO (0 %) (0.94 e^-) models, which demonstrates, in combination with the observed charge density differences, that the strained Sc—Cu interface serves as a catalytically more active site that can effectively stabilize the *OCCO intermediate. To evaluate the *OCCO binding affinity, the projected density of states (PDOS) was calculated for each catalyst model in the absence of surface-adsorbed intermediates (Figs. 5d-f). The Sc_1CuO (1.5

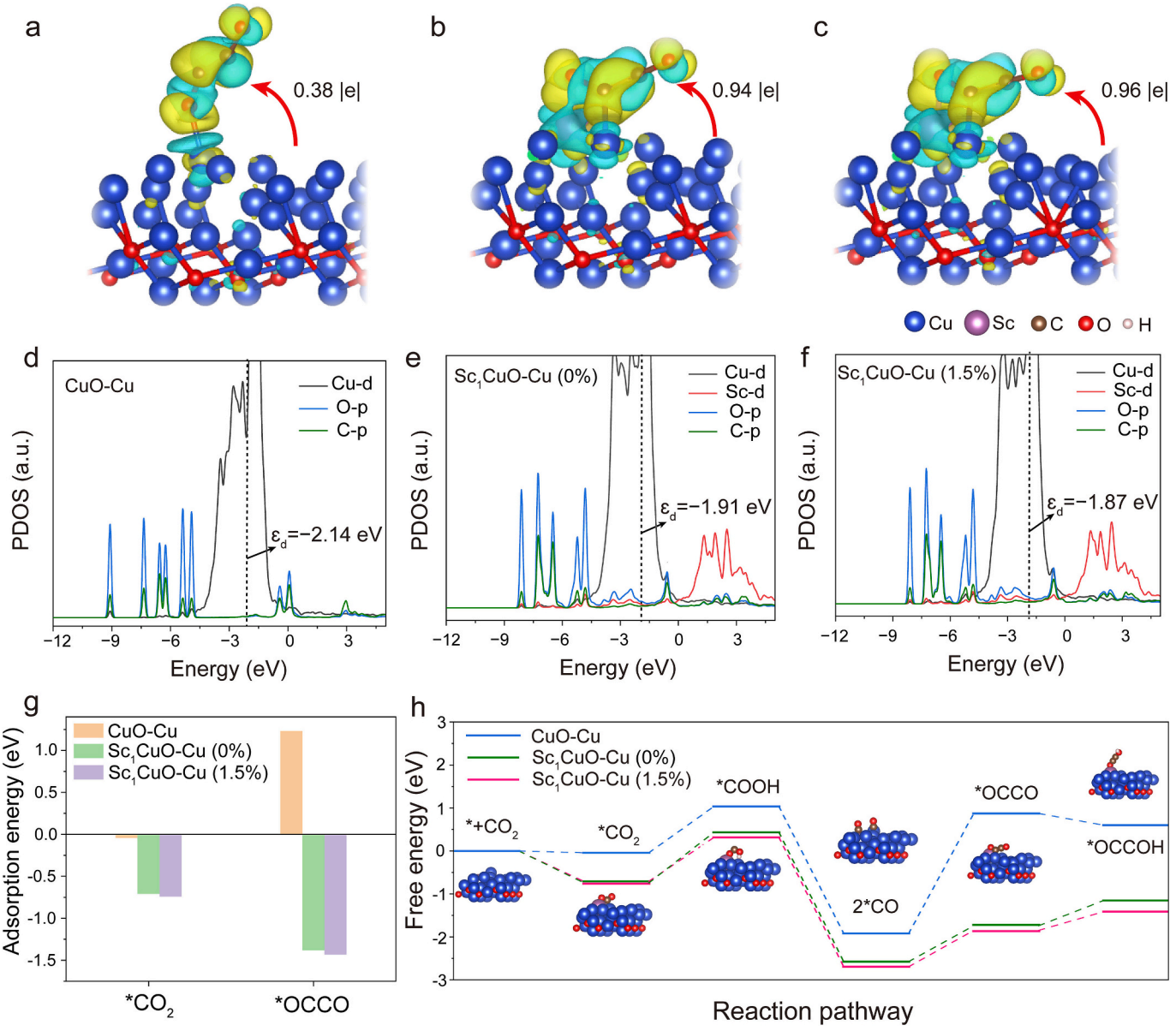

Fig. 5. Charge density difference maps of *OCCO-adsorbed surfaces on (a) reduced CuO (CuO-Cu), (b) Sc_1CuO-Cu (0 %) and (c) Sc_1CuO-Cu (1.5 %). Cyan and yellow regions denote electron depletion and accumulation, respectively. (d-f) PDOS of the *OCCO-adsorbed surfaces for (d) CuO-Cu, (e) Sc_1CuO-Cu (0 %) and (f) Sc_1CuO-Cu (1.5 %). (g) Adsorption energies of $*CO_2$ and *OCCO on CuO-Cu, Sc_1CuO-Cu (0 %) and Sc_1CuO-Cu (1.5 %). (h) Calculated Gibbs free energy diagrams for the CO_2RR taking place on different model catalysts. The blue, purple, brown, red and pink spheres represent Cu, Sc, C, O and H atoms, respectively.

%) catalyst exhibits an upshifted Cu d-band center (−1.87 eV) relative to Sc_1CuO (0 %) (−1.91 eV) and CuO (−2.14 eV), positioning it closer to the Fermi level. Such electronic structure modification indicates enhanced interaction between Sc_1CuO (1.5 %) and the *OCCO intermediate, consistent with its experimentally observed superior catalytic performance. Moreover, the adsorption energies of $*CO_2$ and *OCCO intermediates on CuO, Sc_1CuO (0 %) and Sc_1CuO (1.5 %) were computed (Fig. 5g). The Sc-doped samples show significantly stronger $*CO_2$ adsorption compared to pure CuO, demonstrating the crucial role of Sc doping in CO_2 activation. Moreover, Sc_1CuO (1.5 %) exhibits a higher *OCCO adsorption energy (−1.43 eV) than Sc_1CuO (0 %) (−1.38 eV), indicating that the induced tensile strain is conducive to *OCCO adsorption and also likely promotes its hydrogenation to *OCCOH [42]. Furthermore, the Gibbs free energy profiles for the *CO dimerization pathway are plotted and compared among all model catalysts (Fig. 5h, Table S6), with the corresponding adsorption configurations of $*CO_2$, *COOH, 2*CO, and *OCCO on CuO and Sc_1CuO (0 %) surfaces shown in Figs. S21 and S22. Notably, the first step (i.e., CO_2 adsorption) is an exothermic process on both Sc_1CuO (0 %) and Sc_1CuO (1.5 %) surfaces, showing significantly lowered energy barriers compared to the CuO surface. These theoretical calculations are fully consistent with our experimental findings, demonstrating that Sc doping indeed enhances both CO_2 activation and conversion efficiency. Additionally, the kinetic barrier for the rate-determined step (RDS), i.e., 2*CO-to-*OCCO conversion, is dramatically reduced from 2.78 e*V* for pure CuO to 0.83 eV for Sc_1CuO (0 %), with a further decrease to 0.75 eV for the strained Sc_1CuO (1.5 %). The results unequivocally demonstrate that the tensile strain and abundant undercoordinated Cu^0 sites induced by Sc doping and in-situ electrochemical reduction of CuO synergistically enhance $*CO_2$ adsorption and substantially lower the C—C coupling energy barrier, thereby promoting selective C_{2+} formation.

4. Conclusion

In summary, we successfully synthesized Sc single-atom doped CuO nanosheet catalysts through a simple hydrothermal method and comprehensively investigated how the Sc content influences the electrocatalytic CO_2RR performance. We found that Sc atoms are singly dispersed in the lattice of CuO and the Sc_1CuO NS with an optimal Sc dopant concentration, i.e., Sc_1CuO-1.6, shows outstanding electrocatalytic performance for the CO_2-to-C_{2+} conversion. Specifically, Sc_1CuO-1.6 can achieve a remarkable C_{2+} Faradaic efficiency of 73 ± 1.8 % at 475.2 mA cm^{-2} under an ultralow applied potential of −0.6 V vs. RHE and deliver a high current density of 1.0 A cm^{-2} at a potential of merely −0.88 V vs. RHE, though the Faradaic efficiency is compromised in this case. Comprehensive spectroscopy studies revealed that the in-situ electrochemical reduction of CuO leads to the formation of undercoordinated Cu^0 defect sites in the form of Sc-(O)-Cu coordination motifs, serving as the active centers for CO_2RR under operating conditions. Moreover, Sc doping was confirmed to promote CO_2 activation and stabilize *OCCO — the key intermediate of C_{2+} products. DFT calculations further confirm that Sc doping and the tensile strain caused by oxygen removal facilitate the adsorption of key reaction intermediates and substantially reduce the C—C coupling energy barrier, thereby promoting selective CO_2-to-C_{2+} conversion. Our work provides a guideline for designing high-performance CO_2RR catalysts, and the Sc_1CuO-1.6 catalysts reported herein hold significant potential for producing highly valuable C_{2+} chemicals through CO_2RR.

CRediT authorship contribution statement

Yang Zhao: Writing – original draft, Methodology, Investigation, Formal analysis, Data curation, Conceptualization. **Binwen Zeng:** Validation, Software, Methodology, Formal analysis, Data curation. **Haoliang Huang:** Methodology, Investigation, Formal analysis, Data curation. **Huanhuan Yang:** Validation, Software. **Zhipeng Yu:** Investigation. **Chao Song:** Formal analysis. **Jingwei Wang:** Formal analysis. **Kaiyang Xu:** Visualization, Formal analysis. **Xinyi Xiang:** Formal analysis. **Wei Wang:** Formal analysis. **Fei Lin:** Formal analysis. **Sheng Meng:** Supervision, Software, Resources. **Lijian Meng:** Formal analysis. **Zhiming Cui:** Writing – review & editing, Supervision, Resources. **Lifeng Liu:** Writing – review & editing, Supervision, Resources, Project administration, Funding acquisition, Formal analysis, Conceptualization.

Declaration of competing interest

The authors declare that they have no known competing financial interests or personal relationships that could have appeared to influence the work reported in this paper.

Acknowledgements

L. Liu acknowledges the financial support from the Ministry of Science and Technology of China through the Talent Recruitment Programme (grant No. 22J4021Z311) and the start-up grant of the Songshan Lake Materials Laboratory (grant No. Y2D1051Z311). H. L. Huang would like to thank the financial support of the National Natural Science Foundation of China (grant No. 22309199). The authors thank the BL16U1 (https://cstr.cn/31124.02.SSRF.BL16U1) and BL14W1 (https://cstr.cn/31124.02.SSRF.BL14W1) beamlines of the Shanghai Synchrotron Radiation Facility for the assistance in XAS measurements.

Appendix A. Supplementary data

Supplementary data to this article can be found online at https://doi.org/10.1016/j.cej.2025.169132.

Data availability

Data will be made available on request.

References

[1] P. De Luna, C. Hahn, D. Higgins, S.A. Jaffer, T.F. Jaramillo, E.H. Sargent, What would it take for renewably powered electrosynthesis to displace petrochemical processes? Science 364 (2019) eaav3506.
[2] B.M. Tackett, E. Gomez, J.G. Chen, Net reduction of CO_2 via its thermocatalytic and electrocatalytic transformation reactions in standard and hybrid processes, Nat Catal 2 (2019) 381–386.
[3] B. Cao, F.-Z. Li, J. Gu, Designing Cu-based tandem catalysts for CO_2 electroreduction based on mass transport of CO intermediate, ACS Catal. 12 (2022) 9735–9752.
[4] H. Wu, H. Yu, Y.L. Chow, P.A. Webley, J. Zhang, Toward durable CO_2 electroreduction with Cu-based catalysts via understanding their deactivation modes, Adv. Mater. 36 (2024) 2403217.
[5] Z. Wang, L. Xu, Y. Zhou, Y. Liang, J. Yang, D. Wu, S. Zhang, X. Han, X. Shi, J. Li, Y. Yuan, P. Deng, X. Tian, Stabilizing the oxidation state of catalysts for effective electrochemical carbon dioxide conversion, Chem. Soc. Rev. 53 (2024) 6295–6321.
[6] H. Wang, H.X. Yang, Y.N. Xu, H.Q. Fu, X.Y. Li, J.J. He, Q. Niu, J.C. Wu, H.Y. Yuan, P.F. Liu, H. Yang, Retained oxygen regulation in oxide-derived copper for promoted CO_2 electroreduction towards multi-carbon products, Angew. Chem. Int. Ed. 64 (2025) e202423889.
[7] X. Ma, T. Yang, D. He, X. Gao, W. Jiang, D. Li, Y. Sun, X. Lin, J. Xu, H. Wang, X. Tai, Y. Lin, T. Yao, H. Zhou, Y. Wu, Carbonate shell regulates CuO surface reconstruction for enhanced CO_2 electroreduction, Nat Synth 4 (2024) 53–66.
[8] C.D. Yang, Y. Gao, T. Ma, M.R. Bai, C. He, X.C. Ren, X.L. Luo, C.Z. Wu, S. Li, C. Cheng, Metal alloys-structured electrocatalysts: Metal-metal interactions, coordination microenvironments, and structural property-reactivity relationships, Adv. Mater. 35 (2023) 2301836.
[9] Y. Zhao, Y. Wang, Z. Yu, C. Song, J. Wang, H. Huang, L. Meng, M. Liu, L. Liu, Gold single atom doped defective nanoporous copper octahedrons for electrocatalytic reduction of carbon dioxide to ethylene, ACS Nano 19 (2025) 4505–4514.
[10] J. Changlong Xiao, Zhang, Architectural design for enhanced C_2 product selectivity in electrochemical CO_2 reduction using Cu-based catalysts: A review, ACS Nano 15 (2021) 7975–8000.
[11] Y. Song, X. Zhang, Z. Xiao, Y. Wang, P. Yi, M. Huang, L. Zhang, Coupled amorphous NiFeP/cystalline Ni_3S_2 nanosheets enables accelerated reaction kinetics for high current density seawater electrolysis, Appl. Catal. B Environ. 352 (2024) 124028.

[12] L. Bian, Y. Bai, J.-Y. Chen, H.-K. Guo, S. Liu, H. Tian, N. Tian, Z.-L. Wang, Hierarchical Tandem Catalysis Promotes CO Spillover and Trapping for Efficient CO2 Reduction to C2+ Products, ACS Nano 19 (2025) 9304–9316.
[13] H. Tian, J.-T. Yang, X. Wang, H. Jiao, Z.-F. Gao, K.-Y. Zhu, Q. He, Z.-L. Wang, Ionic liquid-TiO2-CuOx composite interfaces combined with gas directional transmission for enhanced electrooxidation of methane to ethanol, Appl. Catal. B Environ. 375 (2025) 125411.
[14] S.Y. Zhang, W.D. Ruan, J.Q. Guan, Strain effects in carbon dioxide electroreduction, Adv. Energy Mater. 15 (2024) 2404057.
[15] Qichen Wang, D. Yongpeng Lei, Y. Li Wang, Defect engineering in earth-abundant electrocatalysts for CO_2 and N_2 reduction, Energy Environ. Sci. 12 (2019) 1730–1750.
[16] M. Luo, Z. Zhao, Y. Zhang, Y. Sun, Y. Xing, F. Lv, Y. Yang, X. Zhang, S. Hwang, Y. Qin, J.Y. Ma, F. Lin, D. Su, G. Lu, S. Guo, PdMo bimetallene for oxygen reduction catalysis, Nature 574 (2019) 81–85.
[17] R. Chen, Y. Jiang, Y. Zhu, L. Zhang, Y. Li, C. Li, Atomically dispersed scandium in cuprous oxide weakens *CO adsorption to boost carbon dioxide electroreduction toward C_2 products, Adv. Funct. Mater. 35 (2024) 2415940.
[18] C. Li, P. Wang, M. He, X. Yuan, Z. Fang, Z. Li, Rare earth-based nanomaterials in electrocatalysis, Coord. Chem. Rev. 489 (2023) 215204.
[19] Y. Cao, X. Zheng, Y. Deng, W. Hu, Comprehensive insight into electronic modulation of rare-earth elements for enhancing electrocatalytic performance of atomically dispersed materials, Adv. Funct. Mater. 35 (2025) 2423158.
[20] Y. Xue, P. Wang, M. He, T. Zhang, C. Yang, Z. Li, Rare earth nanomaterials in electrochemical reduction of carbon dioxide, Coord. Chem. Rev. 516 (2024) 215983.
[21] J. Zhao, P. Zhang, T. Yuan, D. Cheng, S. Zhen, H. Gao, T. Wang, Z.J. Zhao, J. Gong, Modulation of $*CH_xO$ adsorption to facilitate electrocatalytic reduction of CO_2 to CH_4 over Cu-based catalysts, J. Am. Chem. Soc. 145 (2023) 6622–6627.
[22] J. Liu, P. Li, S. Jia, Y. Wang, L. Jing, Z. Liu, J. Zhang, Q. Qian, X. Kang, X. Sun, Q. Zhu, B. Han, Electrocatalytic CO_2 hydrogenation to C_{2+} alcohols catalysed by Pr–Cu oxide heterointerfaces, Nat Synth 4 (2025) 730–743.
[23] X.P. Yang, Z.Z. Wu, Y.C. Li, S.P. Sun, Y.C. Zhang, J.W. Duanmu, P.G. Lu, X. L. Zhang, F.Y. Gao, Y. Yang, Y.H. Wang, P.C. Yu, S.K. Li, M.R. Gao, Atomically dispersed cerium on copper tailors interfacial water structure for efficient CO-to-acetate electroreduction, Nat. Commun. 16 (2025) 2811.
[24] Q. Wang, T. Luo, X. Cao, Y. Gong, Y. Liu, Y. Xiao, H. Li, F. Gröbmeyer, Y.-R. Lu, T.-S. Chan, C. Ma, K. Liu, J. Fu, S. Zhang, C. Liu, Z. Lin, L. Chai, E. Cortes, M. Liu, Lanthanide single-atom catalysts for efficient CO_2-to-CO electroreduction, Nat. Commun. 16 (2025) 2985.
[25] J. Feng, L. Wu, X. Song, L. Zhang, S. Jia, X. Ma, X. Tan, X. Kang, Q. Zhu, X. Sun, B. Han, CO_2 electrolysis to multi-carbon products in strong acid at ampere-current levels on La-Cu spheres with channels, Nat. Commun. 15 (2024) 4821.
[26] J. Feng, L. Wu, S. Liu, L. Xu, X. Song, L. Zhang, Q. Zhu, X. Kang, X. Sun, B. Han, Improving CO_2-to-C_{2+} product electroreduction efficiency via atomic lanthanide dopant-induced tensile-strained CuO_x catalysts, J. Am. Chem. Soc. 145 (2023) 9857–9866.
[27] Y. Xiao, F. Yu, C. Xia, D. Zhu, J. Chen, N. Liu, Y. Zhao, R. Qi, W. Guo, B. You, T. Yao, Y. Pang, Z. Wang, H. Wang, F. Song, B.Y. Xia, Asymmetric CO–CHO coupling over Pr single-atom alloy enables industrial-level electrosynthesis of ethylene, J. Am. Chem. Soc. 147 (2025) 15654–15665.
[28] Y. Jiang, Z. Liang, H. Fu, C. Gu, Y. Du, High-entropy rare earth oxides anchoring tunable $Cu^{\delta+}$ nanochimneys for self-tandem C-C coupling catalysis, Adv. Mater. 2503027 (2025).
[29] P. Wang, S. Meng, B. Zhang, M. He, P. Li, C. Yang, G. Li, Z. Li, Sub-1 nm Cu_2O nanosheets for the electrochemical CO_2 reduction and valence state–activity relationship, J. Am. Chem. Soc. 145 (2023) 26133–26143.
[30] Y. Zang, T. Liu, P. Wei, H. Li, Q. Wang, G. Wang, X. Bao, Selective CO_2 electroreduction to ethanol over a carbon-coated CuO_x catalyst, Angew. Chem. Int. Ed. 61 (2022) e202209629.
[31] E.P. Delmo, Y. Wang, Y. Song, S. Zhu, H. Zhang, H. Xu, T. Li, J. Jang, Y. Kwon, Y. Wang, M. Shao, In situ infrared spectroscopic evidence of enhanced electrochemical CO_2 reduction and C–C coupling on oxide-derived copper, J. Am. Chem. Soc. 146 (2024) 1935–1945.
[32] S.B. Liu, X.F. Lu, J. Xiao, X. Wang, X.W. Lou, Bi_2O_3 nanosheets grown on multi-channel carbon matrix to catalyze efficient CO_2 electroreduction to HCOOH, Angew. Chem. Int. Ed. 58 (2019) 13828–13833.
[33] S. Gao, Z. Sun, W. Liu, X. Jiao, X. Zu, Q. Hu, Y. Sun, T. Yao, W. Zhang, S. Wei, Y. Xie, Atomic layer confined vacancies for atomic-level insights into carbon dioxide electroreduction, Nat. Commun. 8 (2017) 14503.
[34] Z. Lian, F. Dattila, N. López, Stability and lifetime of diffusion-trapped oxygen in oxide-derived copper CO_2 reduction electrocatalysts, Nat. Catal. 7 (2024) 401–411.
[35] Y. Yang, S. Louisia, S. Yu, J. Jin, I. Roh, C. Chen, M.V. Fonseca Guzman, J. Feijoo, P.C. Chen, H. Wang, C.J. Pollock, X. Huang, Y.T. Shao, C. Wang, D.A. Muller, H. D. Abruna, P. Yang, Operando studies reveal active Cu nanograins for CO_2 electroreduction, Nature 614 (2023) 262–269.
[36] Z. Li, Y. Wang, H. Liu, Y. Feng, X. Du, Z. Xie, J. Zhou, Y. Liu, Y. Song, F. Wang, M. Sui, Y. Lu, F. Fang, D. Sun, Electroreduction-driven distorted nanotwins activate pure Cu for efficient hydrogen evolution, Nat. Mater. 24 (2025) 424–432.
[37] Y. Zhang, Y. Chen, X. Wang, Y. Feng, Z. Dai, M. Cheng, G. Zhang, Low-coordinated copper facilitates the $*CH_2CO$ affinity at enhanced rectifying interface of Cu/Cu_2O for efficient CO_2-to-multicarbon alcohols conversion, Nat. Commun. 15 (2024) 5172.
[38] Y. Wang, Y. Cheng, S. Liu, Y. Yin, J. Yang, H. Wang, K. Li, M. Zhou, J. Jiao, P. Zhang, Q. Qian, Q. Zhu, X. Sun, Y. Xu, M. Luo, X. Kang, B. Han, Enhancing CO_2 eelectroreduction to multicarbon pproducts by modulating the surface microenvironment of electrode with polyethylene glycol, Angew. Chem. Int. Ed. 64 (2025) e202420661.
[39] D. Wei, Y. Wang, C.L. Dong, Z. Zhang, X. Wang, Y.C. Huang, Y. Shi, X. Zhao, J. Wang, R. Long, Y. Xiong, F. Dong, M. Li, S. Shen, Decrypting the controlled product selectivity over Ag-Cu bimetallic surface alloys for electrochemical CO_2 reduction, Angew. Chem. Int. Ed. 62 (2023) e202217369.
[40] S. Wang, F. Li, J. Zhao, Y. Zeng, Y. Li, Z.-Y. Lin, T.-J. Lee, S. Liu, X. Ren, W. Wang, Y. Chen, S.-F. Hung, Y.-R. Lu, Y. Cui, X. Yang, X. Li, Y. Huang, B. Liu, Manipulating C-C coupling pathway in electrochemical CO_2 reduction for selective ethylene and ethanol production over single-atom alloy catalyst, Nat. Commun. 15 (2024) 10247.
[41] Z. Wei, W. Wang, T. Shao, S. Yang, C. Liu, D. Si, R. Cao, M. Cao, Constructing Ag/Cu_2O interface for efficient neutral CO_2 electroreduction to C_2H_4, Angew. Chem. Int. Ed. 64 (2025) e202417066.
[42] C. Long, X. Liu, K. Wan, Y. Jiang, P. An, C. Yang, G. Wu, W. Wang, J. Guo, L. Li, K. Pang, Q. Li, C. Cui, S. Liu, T. Tan, Z. Tang, Regulating reconstruction of oxide-derived Cu for electrochemical CO_2 reduction toward n-propanol, Sci. Adv. 9 (2023) eadi6119.
[43] Q. Sun, X. Tan, C. Jia, C. Rong, S. Wang, C. Han, Y. Xiao, H. Qi, S.C. Smith, C. Zhao, Molecule doping of atomically dispersed Cu–Au alloy for enhancing electroreduction of CO to C_{2+} products, Adv. Funct. Mater. 34 (2024) 2406281.
[44] S. Li, G. Zhang, X. Ma, H. Gao, D. Fu, T. Wang, J. Zeng, Z.-J. Zhao, P. Zhang, J. Gong, Atomically isolated Pd sites promote electrochemical CO reduction to acetate through a protonation-regulated mechanism, J. Am. Chem. Soc. 146 (2024) 31927–31934.
[45] X. Wu, Z. Tong, Y. Liu, Y. Li, Y. Cheng, J. Yu, P. Cao, C. Zhuang, Q. Shi, N. Liu, X. Liu, H. Liang, H. Li, Modification of the CuO electronic structure for enhanced selective electrochemical CO_2 reduction to ethylene, Nano Res 17 (2024) 7194–7202.